JOURNAL OF GEOPHYSICAL RESEARCH, VOL. 113, C03032, doi:10.1029/2007JC004496, 2008

The mean seasonal cycle in sea level estimated from a data-constrained general circulation model

Sergey V. Vinogradov,[1] Rui M. Ponte,[1] Patrick Heimbach,[2] and Carl Wunsch[2]

Received 9 August 2007; revised 19 October 2007; accepted 6 December 2007; published 29 March 2008.

[1] A near-global ocean state estimate over the period 1992–2004 is used to study the mean seasonal cycle in sea level ζ. The state estimate combines most available observations, including all the altimetric missions, with a general circulation model in an optimization procedure. The annual cycle tends to be larger than the semi-annual one, except in tropical regions. For global mean ζ, annual thermosteric and freshwater terms are nearly out-of-phase and lead to an annual cycle of only a few mm in amplitude. Regionally, surface wind stress and heat flux are the primary drivers for seasonal ζ variations in the tropics and midlatitudes, respectively, with both mechanisms playing a role at high latitudes. A substantial part of the annual ζ variability can be assigned to changes in thermosteric height in the upper 100 m in midlatitudes and 200 m in the tropics. Bottom pressure variability is larger at high latitudes, and also in some regions in the Southern Ocean and North Pacific. Apparent nonlinear rectification processes lead to a noticeable impact of submonthly forcing on the annual cycle in the western North Atlantic and North Pacific. Other features include the substantial ζ gradients associated with strong spatial variability in seasonal surface heat flux in some western boundary regions, the damping effects of surface heat flux on the seasonal cycle in the tropics, and the importance of wind driving and bottom pressure in shallow regions, which can cause differences in the seasonal cycle in some coastal and contiguous deep-ocean regions.

Citation: Vinogradov, S. V., R. M. Ponte, P. Heimbach, and C. Wunsch (2008), The mean seasonal cycle in sea level estimated from a data-constrained general circulation model, *J. Geophys. Res.*, *113*, C03032, doi:10.1029/2007JC004496.

1. Introduction

[2] Sea level variability is a subject of major scientific study and continuous observations, given its crucial role in human activities that are increasingly concentrated on the coastal zones of the world's oceans. Sea level is also a major climate indicator as it relates to ocean heat content, surface currents, and other important parameters defining the Earth's climate. Of the many low-frequency signals in the sea level record, the seasonal cycle is particularly ubiquitous and prominent, and its understanding continues to be an important goal of climate research.

[3] Following earlier studies, sea level (ζ) can be written as

$$\zeta = \frac{p_b}{\rho_s g} - \int_{-H}^{0} \frac{\rho}{\rho_s} dz = \zeta_m + \zeta_\rho \qquad (1)$$

where p_b is bottom pressure, ρ_s is ocean surface density, g is the acceleration of gravity, and H is depth. (A complete list of notations used in the paper is provided in Table 1.) Variability in ζ with respect to the geoid arises from changes in steric height ζ_ρ, due to changes in temperature (thermosteric height ζ_ρ^T) and freshwater content (halosteric height ζ_ρ^S), and mass variations ζ_m, related to redistribution of mass within the ocean and mass input from precipitation, evaporation and river runoff. In (1), we have ignored atmospheric pressure loading effects that give rise to substantial but dynamically irrelevant changes in ζ at the seasonal timescale, through the so-called inverted barometer effect [e.g., *Ponte*, 2006]. Similarly ignored in this study are the ζ signals, of order 1 cm, associated with the annual and semi-annual tides [e.g., *Wunsch*, 1967].

[4] Early estimates of the ζ seasonal cycle by *Patullo et al.* [1955], later updated by *Tsimplis and Woodworth* [1994], were based on the sparse tide gauge data set, including mainly coastal records and a few open-ocean (island) records. The annual phase reversal in ζ between northern and southern hemispheres was noticed early, as well as the significance of ζ_ρ to the seasonal variability in ζ. The sparse tide gauge network could not resolve, however, the full detail of the large-scale seasonal ζ patterns. *Gill and Niiler* [1973] showed the importance of surface heat flux to seasonal changes in ζ at midlatitudes, in the first attempt to map average seasonal changes in ζ_m and upper ocean ζ_ρ for the North Atlantic and North Pacific.

[5] Developments in satellite altimetry in the 1990s brought the capability to observe ζ on global scales and sparked many studies of the seasonal ζ variability [e.g.,

[1] Atmospheric and Environmental Research, Inc., Lexington, Massachusetts, USA.
[2] Massachusetts Institute of Technology, Cambridge, Massachusetts, USA.

0148-0227/08/2007JC004496$09.00

Table 1. Symbols Used in the Text

Variable	Definition
ζ	sea level
ζ_m	bottom pressure equivalent sea level
ζ_ρ	steric height
ζ_ρ^T	thermosteric height
ζ_ρ^S	halosteric height
p_b	bottom pressure
H	depth
ρ_s	ocean surface density
E_S	surface freshwater flux
$\mathcal{H}$	surface heat flux
τ	surface wind stress
$\overline{(\cdot)}$	spatial averaging operator applied for the global ocean

Jacobs et al., 1992; *Fu and Smith*, 1996; *Stammer*, 1997; *Fukumori et al.*, 1998; *Ferry et al.*, 2000; *Pierini*, 2003; *Vivier et al.*, 1999, 2005; *Fu*, 2007]. Apart from confirming the importance of ζ_ρ and air-sea heat exchange at mid latitudes described by *Gill and Niiler* [1973], these studies began to reveal the overall spatial complexity of the seasonal ζ variability and the richness of its dynamics, involving horizontal and vertical advection of heat, wave propagation, and barotropic processes associated with wind driving. Most of these works use only a few years of altimeter data, however, and comparisons with various models and other data sets often led to ambiguous interpretation of the observations (e.g., differences in ζ and ζ_ρ could indicate uncertainties in either data or model estimates of these quantities or the importance of ζ_m changes). Altimetry also permitted the study of the seasonal cycle in global mean sea level $\overline{\zeta}$ [*Chen et al.*, 1998, 2005; *Minster et al.*, 1999; *Chambers et al.*, 2004], but interpretation of results is equally difficult owing to the lack of estimates of mean steric height or freshwater contributions that are fully consistent with ζ estimates in terms of spatial and temporal coverage.

[6] The development of state-of-the-art ocean circulation models and advanced state estimation techniques make possible near-global estimates of the ocean state that are a best fit to most available oceanographic observations. Besides making the best use of the space-born radar altimetry in conjunction with hydrographic profiles, drifters, and all the other in situ and satellite data, such products provide hydrodynamically consistent fields of ζ, temperature, and salinity that can be used to compute ζ_ρ and ζ_m contributions, either regionally or globally. Surface atmospheric fluxes can also be estimated within the same data-constrained ocean model framework, which provides a new tool to study the dynamics and forcing of ζ variations, on regional and global scales. In this paper, we examine the mean ζ seasonal cycle from 13 years of a data-constrained ocean state estimate derived as part of the ECCO-GODAE project (Estimating the Circulation and Climate of the Ocean-Global Ocean Data Assimilation Experiment) [*Wunsch and Heimbach*, 2007]. The ECCO-GODAE estimate covers the period from 1992 to 2004 which coincides with the bulk of the World Ocean Circulation Experiment (WOCE, e.g., *Siedler et al.* [2001]). The model is constrained to virtually all existing altimetric data, but also to most other available ocean observations. It permits a comprehensive study of ζ and the relative contributions from ζ_ρ and ζ_m, the horizontal and vertical structure of variability, and the relevant forcing and dynamics. The ECCO-GODAE estimate is described in section 2, together with a comparison to altimetric data. Sections 3 and 4 describe the seasonal variability in $\overline{\zeta}$ and ζ, respectively. Interpretation and discussion of results in terms of relevant forcing and dynamics is presented in section 5, followed by a summary.

2. Methods

[7] The ECCO-GODAE optimization procedure uses an evolved version of the MIT general circulation model [*Marshall et al.*, 1997a, 1997b] and its adjoint [*Heimbach et al.*, 2005] to produce an estimate of the ocean state (temperature, salinity, currents and sea level) and corresponding surface atmospheric forcing fields (wind stress, heat and freshwater flux) that are a least squares fit to numerous types of oceanographic observations (altimetry, P-ALACE/Argo autonomous floats, CTD/XBT, etc., currently more than 100 million data points; see *Wunsch and Heimbach* [2007], for a complete description). The model solves the Boussinesq form of the Navier-Stokes equations for an incompressible fluid, in height coordinates, using parameterizations of the sub-grid processes and mixed layer. In the present configuration, the model uses a virtual salt flux surface boundary condition and a linear free surface approximation, which produce consistent budgets of salt and surface freshwater input (*Wunsch et al.* [2007] discuss six different surface boundary conditions in use for salt/freshwater in relation to the accuracy of ζ trend estimates, but for the shorter, seasonal time scales, the choice of a particular formulation may not be as important). The model domain is quasi-global covering 80°S to 80°N with $1° \times 1°$ spatial resolution and 23 non-uniformly spaced layers in the vertical.

[8] The model was spun up for one month using December climatological initial conditions for temperature and salinity based on the World Ocean Atlas (WOA94, *Levitus and Boyer* [1994]), and forced with December 1991 air-sea fluxes. This provides an essentially geostrophically adjusted initial velocity field for the subsequent optimization. As part of the control space, the initial temperature and salinity fields are then adjusted together with the time-varying air-sea fluxes such as to produce an optimal fit to the observations. The atmospheric surface forcing is the 6-hourly fields of the NCEP/NCAR (National Centers for Environmental Prediction/National Center for Atmospheric Research) reanalysis [*Kalnay et al.*, 1996]. The ECCO-GODAE optimization is an iterative process, and this study is based on the monthly averaged results from version 2, iteration 177, produced at MIT and AER and used in the study by *Wunsch and Heimbach* [2006]. Further details on the ECCO-GODAE solutions are discussed by *Heimbach et al.* [2006], *Wunsch and Heimbach* [2007], and references therein. An important feature of these estimates is that they are obtained from the forward model, running freely under adjustments to the control vector, and so not containing any artificial temporal discontinuities or fictitious energy sources.

[9] Daily along-track altimeter ζ data from TOPEX/POSEIDON/Jason-1 (TPJ), ERS, EnviSat, and GFO, are interpolated on the model grid, and used to constrain the

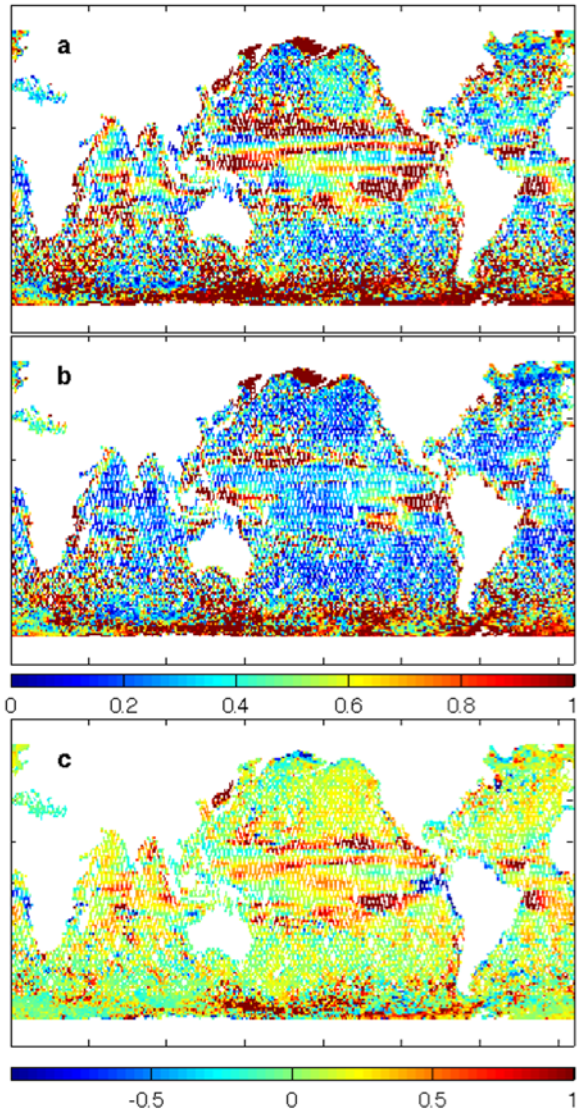

Figure 1. Root-mean square difference between the mean annual cycles in the TPJ data and (a) the control run, (b) the optimized solution, both normalized by the RMS variability in the TPJ annual cycle. The difference (a)-(b) is shown in Figure 1c. All annual harmonics are calculated based on 12 climatological monthly means.

solution, but only in areas where $H > 1000$ m, to avoid coastal regions where data errors are considerably larger. The overall goal of the optimization procedure is to bring the solution closer to observations, according to the assigned weights based on the estimated data errors (for altimeter error estimates, see *Ponte et al.* [2007a]). To briefly illustrate the effects of the optimization, Figure 1 examines the RMS (root mean square) differences between mean annual cycles in constrained or unconstrained (control run) solutions and the high quality TPJ data; results are normalized by the annual RMS variability in the TPJ data. Annual signals in the unconstrained solution are close to ones in TPJ, however there are many areas (e.g., tropics, Southern Ocean) where the model-data misfits are as large as the TPJ variability (Figure 1a). The optimized solution is much closer to the TPJ data than the control run (Figure 1b) in most of the ocean, and particularly in the tropics. Figure 1c demonstrates the substantial reduction in model-data misfits achieved by the optimization almost everywhere. The mean correlation coefficient between the ζ annual cycle in TPJ and in solution increases from 0.70 in the control run to 0.78 in the optimized solution. For the total ζ variability, including all periods longer than 2 months, the mean correlation increases from 0.42 to 0.59.

[10] The solution misfits relative to TPJ are largest in the high southern latitudes, some areas of the tropical Pacific, and in the vicinity of strong currents. This distribution relates to problems in both model and data. In some of these areas, the altimeter data are downweighted [*Ponte et al.*, 2007a] and the solution pulled closer to hydrographic and other data constraints. The Southern Ocean is a challenging place, with its complex unresolved processes in the vicinity of the Antarctic Circumpolar Current, high uncertainties in the forcing fields, and simply a lack of observations in general, in particular in the sea-ice covered part of the ocean. Larger misfits in coastal regions and semi-enclosed seas can be related to poor resolution of shelves, connecting straits and passages, and the aforementioned altimeter quality issues in the vicinity of land/sea boundaries. As a consequence of large prior uncertainties in these regions, the corresponding misfit terms are effectively downweighted (to the extent that observations exist at all), and the optimization is not expected to lead to significant adjustments there. Comparisons with the independent tide gauge data (not shown) are consistent with these results, showing better agreement in the open ocean than in the coastal regions which are poorly resolved by the model.

[11] As illustrated by the discussion of Figure 1, the optimized solution analyzed here is not perfect, but represents a "best estimate" of the ζ seasonal cycle at present, given all the information contained in the ECCO-GODAE model and data sets. Such estimates are expected to evolve, as model improvements, new data sets, better understanding of errors, and other developments take hold. Nevertheless, the current solution is sufficiently robust to merit detailed analysis of the seasonal variability in ζ, serving as a benchmark for future studies.

[12] Analyses of global and regional ζ are based on the mean climatological annual and semi-annual cycles, using Fourier decomposition of the 12 climatological monthly means obtained by averaging all January, all February, etc., over the 13 years of record. The formal uncertainties in these monthly estimates, based on the intramonthly variability and the number of days ($\sim$400) going into each monthly mean, are typically small compared to the amplitudes of the seasonal cycle. The computed phases are defined as in Table 2.

3. Seasonal Cycle in Global Mean Sea Level

[13] Global mean sea level ($\overline{\zeta}$) is a widely used proxy for heat and freshwater exchange among ocean, atmosphere and land in climate studies. Changes in $\overline{\zeta}$ are mainly related to variations in mean steric height ($\overline{\zeta_\rho}$) and total oceanic mass ($\overline{\zeta_m}$) from net input of freshwater, with atmospheric pressure having a negligible effect (compressibility of seawater does not exceed 1.8% in fractional volume compression even at abyssal depths, e.g., *Halliday et al.* [2004]).

Table 2. Global Mean Sea Level $\overline{\zeta}$, Steric Height $\overline{\zeta_\rho}$, Thermosteric Height $\overline{\zeta_\rho^T}$, Halosteric Height $\overline{\zeta_\rho^S}$, and Bottom Pressure $\overline{\zeta_m}$

$\overline{\zeta}$	Annual			Semi-annual	
Estimates	Amp, mm	Φ° [a]	Peak	Amp, mm	Φ° [a]
$\overline{\zeta_\rho^S}$	0.2	68	22 Oct	0.01	35
$\overline{\zeta_\rho^T}$	3.5	263	7 Apr	1.4	93
$\overline{\zeta_\rho}$	3.4(0.6)	264	6 Apr	1.4(0.3)	92
$\overline{\zeta_m}$: $36.7 \times \zeta_\rho^S$ [b]	5.5(2.2)	68	22 Oct	0.4	35
$\overline{\zeta_m}$: $-\int_0^t \bar{E}_S(\tau)d\tau$ [c]	6.4(2.3)	86	4 Oct	0.8	86
$\overline{\zeta_m}$: TPJ $-$ $\overline{\zeta_\rho}$	8.2	63	27 Oct	0.8	209
$\overline{\zeta}$: $\overline{\zeta_\rho} + 36.7 \times \overline{\zeta_\rho^S}$	2.5	47	12 Nov	1.7	80
$\overline{\zeta}$: $\overline{\zeta_\rho} - \int_0^t \bar{E}_S(\tau)d\tau$	3.0	88	2 Oct	2.2	90
$\overline{\zeta}$: TPJ	5.1(1.5)	48	11 Nov	1.3(0.5)	129
		Other estimates [*Minster et al.*, 1999]			
$\overline{\zeta_\rho}$ (Levitus)	5.0	289	12 Mar		
$\overline{\zeta_m}$ (TPE-Levitus) [d]	9.5	101	19 Sep		
$\overline{\zeta}$ (TPE)	4.6	92	27 Sep		
		Other estimates [*Chambers et al.*, 2004]			
$\overline{\zeta_m}$ (GRACE)	8.6	85	5 Oct		
		Other estimates [*Chen et al.*, 2005]			
$\overline{\zeta_\rho}$ (WOA)	5.3	288	13 Mar	1.7	116
$\overline{\zeta_m}$ (Altimetry-WOA)	8.8	89	1 Oct	0.4	282
$\overline{\zeta_m}$ (GRACE)	7.2	84	6 Oct	1.4	213
$\overline{\zeta}$ (Altimetry)	4.2	64	26 Oct	1.4	120
		Other estimates [*Lombard et al.*, 2007]			
$\overline{\zeta_m}$ (GRACE)	7.3	76	14 Oct		

As an estimate of uncertainty for some of the amplitudes shown, year-to-year change, in terms of standard deviation, is given in parenthesis.
[a]Phase in degrees as in $Amp \times \cos(\omega t + \Phi)$.
[b]Values of $\overline{\zeta_m}$ estimated from the mean halosteric height times the "Munk multiplier".
[c]Values of $\overline{\zeta_m}$ as computed from model estimate of the global mean freshwater flux, $\bar{E}_S(t)$.
[d]TPE is TOPEX/POSEIDON and ERS-1 altimetric missions for 1992–1997.

While many studies have examined long-term trends in $\overline{\zeta}$, our focus here is the mean seasonal cycle. The trend in $\overline{\zeta}$ annual amplitudes is insignificant. Spatial averages are area-weighted, with uncertainties due to spatial averaging not exceeding 3×10^{-3} mm for any sea level component (for more on calculating global averages, see *Wunsch et al.* [2007]). All estimates of annual and semi-annual cycles in $\overline{\zeta}$ discussed here are given in Table 2 with uncertainty estimates for some of the amplitudes provided as year-to-year variability (standard deviation).

[14] Our altimetry-derived $\overline{\zeta}$ series based on monthly gridded TPJ fields yield annual and semi-annual cycles with amplitudes ~5.1 mm and 1.3 mm, respectively, with the annual maximum occurring in mid-November. These estimates are in good agreement with those of *Chen et al.* [2005], which are based on a different altimeter data set and period of analysis. The altimeter observations thus suggest a relatively stable seasonal cycle in $\overline{\zeta}$, dominated by the annual component, and representing both $\overline{\zeta_\rho}$ and $\overline{\zeta_m}$ contributions. (Note that the TPJ product is less dense than the model output and extends to only ±66° latitudinally; such differences in spatial coverage should be kept in mind when comparing model and data $\overline{\zeta}$ values.)

[15] Our estimates of $\overline{\zeta_\rho}$ and $\overline{\zeta_m}$ are different from previous ones because they are computed from the dynamically consistent estimate of the near-global ocean state. For the Boussinesq formulation and virtual salt flux boundary condition used in the current ECCO-GODAE model, the total ocean volume and hence $\overline{\zeta}$ remains constant to within numerical precision, but one can still estimate the steric contributions to $\overline{\zeta}$ from the density fields. Time series of $\overline{\zeta_\rho}$ (integrated over the full water column) yield annual and semi-annual amplitudes of 3.4 mm and 1.4 mm, respectively. The major contributor to $\overline{\zeta_\rho}$ is the thermosteric change, with only sub-millimeter amplitudes in the freshwater part. In addition, integrals to different depths indicate that most of the variability in $\overline{\zeta_\rho}$ is contributed by temperature changes over the upper 200 m, where effects of the seasonally varying heat flux are mostly felt. Compared to the estimates of *Chen et al.* [2005], based on analysis of the World Ocean Atlas (WOA01, *Stephens et al.* [2002]), our $\overline{\zeta_\rho}$ signal has ~20% lower annual and semi-annual amplitudes, and differences in phase of ~24 and 12 days, respectively. Such differences are expected, given the widely disparate methods and period of analysis considered, and the inherent

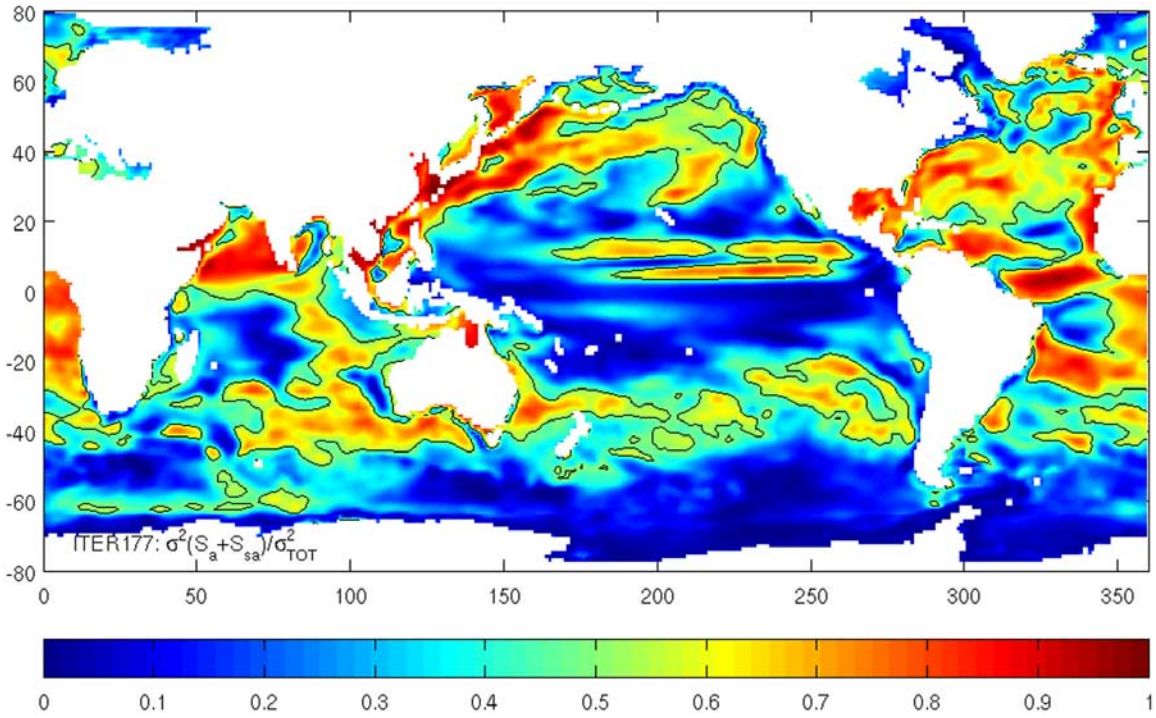

Figure 2. Ratio of the seasonal to total variance of sea level. Seasonal variance is computed from the mean climatological annual plus semi-annual cycles. Total variance is based on all 156 monthly fields, with linear trend retained. Contour line depicts a variance ratio of 0.5.

noise in calculating what amounts to global oceanic averages of temperature and salinity fields.

[16] Variability in $\overline{\zeta_m}$ provides insight into the global hydrological cycle. Time series of $\overline{\zeta_m}$ can be obtained directly by integrating in time the global mean freshwater flux $\overline{E_S}$. In the ECCO-GODAE solution, a priori estimates of freshwater flux fields representing evaporation minus precipitation from the NCEP/NCAR reanalysis and a time-mean river runoff are adjusted as part of the optimization. The resulting estimate of $\overline{\zeta_m}$ exhibits an annual cycle of 6.4 mm in amplitude with a peak in the beginning of October. The semi-annual cycle is much weaker.

[17] A more indirect method to obtain $\overline{\zeta_m}$ is based on the global mean halosteric height $\overline{\zeta_\rho^S}$. *Munk* [2003] demonstrated that, in the absence of sea ice melting, multiplying $\overline{\zeta_\rho^S}$ by the "Munk multiplier", $M = \rho/\Delta\rho$, where ρ is the density of seawater and $\Delta\rho$ is the incremental density of seawater relative to freshwater of the same temperature, provides a good estimate of $\overline{\zeta_m}$. Using M with our estimate of $\overline{\zeta_\rho^S}$ yields an estimate of $\overline{\zeta_m}$ with an annual cycle of 5.5 mm in amplitude and peak in late October, similar to but not the same as the direct estimates from the freshwater flux. Differences between the two methods can be attributed to uncertainties in the value of M, in the equation of state, and in the calculation of the global mean salinity [*Wunsch et al.*, 2007], among other factors. These results suggest that, in practice, the use of $\overline{\zeta_\rho^S}$ to infer $\overline{\zeta_m}$ must be taken with caution, given that any errors are magnified by M.

[18] Values of $\overline{\zeta}$ obtained by summing $\overline{\zeta_\rho}$ and either of our $\overline{\zeta_m}$ estimates yield annual amplitudes smaller than from TPJ alone and also a somewhat different phase for the case of the flux-based estimate of $\overline{\zeta_m}$. Various model issues can contribute to these discrepancies. In particular, the use of a constant runoff and the absence of sea-ice can be a source of model biases. Some of these errors are mitigated by the optimization, but the available salinity data are likely insufficient to constrain the seasonal variability in $\overline{\zeta_\rho^S}$ to submillimeter precision. The possible use of satellite measurements from the Gravity Recovery and Climate Experiment (GRACE) mission to directly constrain $\overline{\zeta_m}$ terms is the subject of ongoing research [*Ponte et al.*, 2007b].

[19] *Minster et al.* [1999] and *Chen et al.* [2005] have estimated $\overline{\zeta_m}$ by differencing the altimetrically observed $\overline{\zeta}$ and the thermosteric component derived from in situ temperature observations, and comparison with those estimates suggest that the annual cycle in $\overline{\zeta_m}$ may be underestimated in our solution. Compared to the GRACE-derived annual $\overline{\zeta_m}$ variability [*Chambers et al.*, 2004; *Chen et al.*, 2005; *Lombard et al.*, 2007], our estimates have similar phases but somewhat weaker amplitudes. Assuming our estimates of $\overline{\zeta_\rho}$ are well determined, the difference between TPJ and our $\overline{\zeta_\rho}$ estimate gives a $\overline{\zeta_m}$ annual amplitude of 8.2 mm with a peak in late October, which is somewhat different from the direct and indirect $\overline{\zeta_m}$ estimates discussed above, but comparable to the estimates by *Chen et al.* [2005] based on different altimeter estimates and WOA. Semi-annual harmonics in both estimates are weak (sub-millimeter).

[20] Ultimately, one must also consider the uncertainties in the altimetry estimates. For example, most of the environmental and model corrections applied to TPJ data have considerable variability at the seasonal timescale, and any associated errors [e.g., *Fernandes et al.*, 2006] are expected to affect the data estimates at the millimeter level of accuracy needed for inferences on $\overline{\zeta}$. The differences

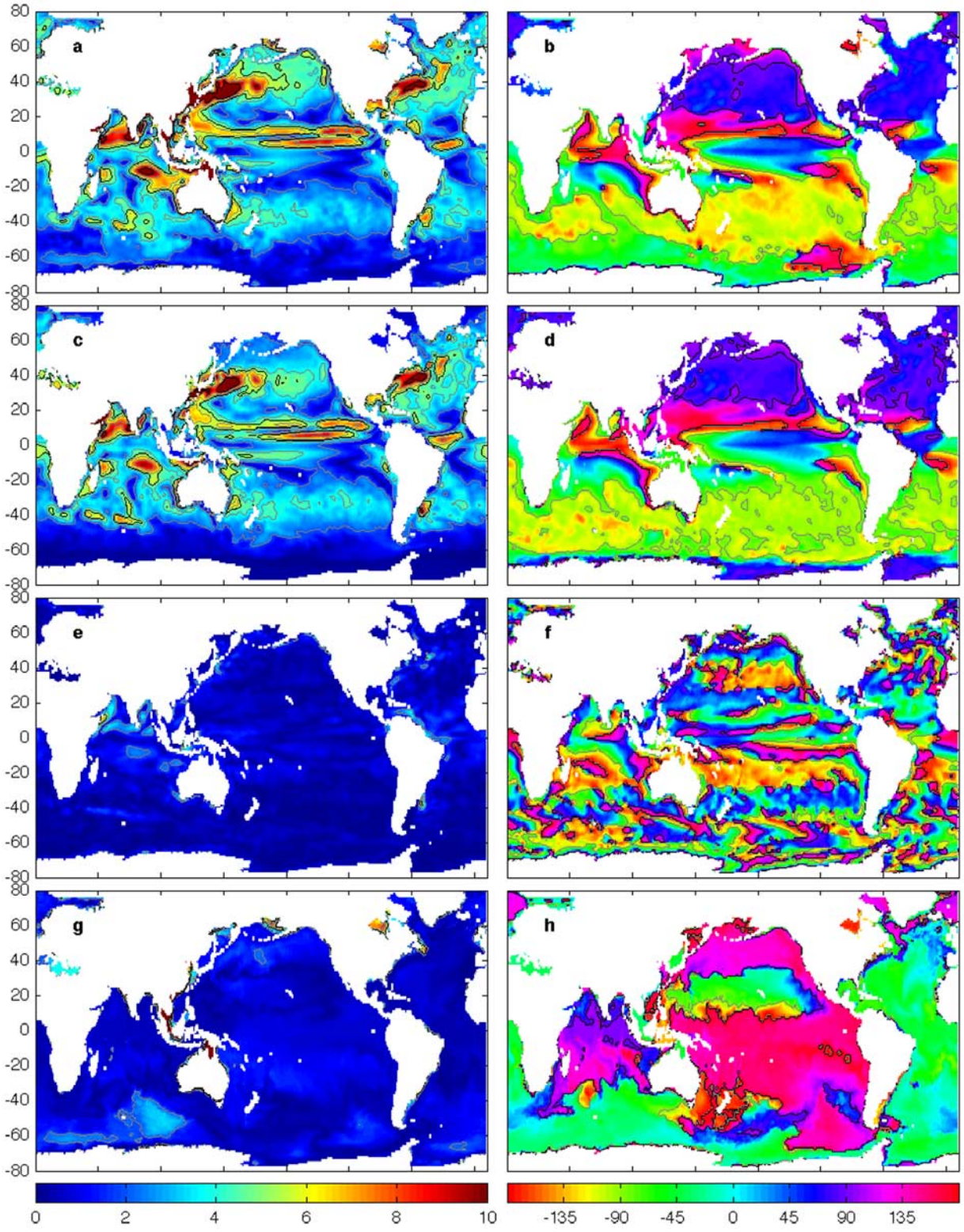

Figure 3. Amplitude (cm, left column) and phase (deg, right column) of the annual cycle in (a, b) modeled sea level, (c, d) thermosteric height ζ_ρ^T, (e, f) halosteric height ζ_ρ^S, and (g, h) bottom pressure or mass term ζ_m. In amplitude plots, solid black contours are plotted every 5 cm and gray contours are plotted every 2 cm. In phase plots, black contour lines are plotted for 90° isolines and gray contour lines for −90° isolines.

between the various estimates of $\overline{\zeta}$, $\overline{\zeta_\rho}$, and $\overline{\zeta_m}$ in Table 2 are likely indicative of the accuracy that can be achieved with present data sets and modeling capabilities.

4. Seasonal Cycle in Regional Sea Level

[21] Dynamically relevant ζ signals, related to surface pressure gradients and currents, are associated with spatially varying patterns. In this section, we examine the regional ζ fluctuations at the seasonal timescale, with the spatial mean effects considered in section 3 excluded. The seasonal cycle is an important component of the local low-frequency ζ variability over most of the ocean. Figure 2 shows the ratio of the variance of the mean seasonal cycle (annual plus semi-annual harmonics) to the total ζ variance based on 156 monthly mean values. Dominance of seasonal variance (>80%) is found in the tropical Indian and Atlantic, and in the northwest Pacific Ocean, but many other tropical and midlatitude areas show values higher than 50%. Areas with relatively weak seasonal variance (<20% of the total variance) are found at high latitudes, particularly in the Southern Ocean, and in the tropical Pacific, where strong interannual and intraseasonal variability are expected. In a broader sense, Figure 2 also gives a measure of the size of the annual and semi-annual periodic signals relative to the background low-frequency continuum. Regions with large ratio indicate a strong narrow-band, periodic signal on top of the stochastic background. As the ratio gets smaller, the seasonal cycle becomes less distinguishable from the broad-band stochastic background. In what follows, we examine the spatial patterns of the seasonal ζ variability in relation to ζ_ρ^T, ζ_ρ^S and ζ_m, and the vertical structure of ζ_ρ signals.

[22] The amplitude of the mean climatological annual cycle in ζ is shown in Figure 3a. Values are mostly less than 10 cm. The strongest amplitudes (10–15 cm) can be found within western boundary currents, particularly in the Kuroshio and Gulf Stream regions, and within narrow zonally elongated bands in the tropical Pacific between 5°N and 15°N. In the tropical Indian Ocean, there are two distinct areas with pronounced high annual amplitudes (~10 cm) near the Cocos (Keeling) Islands and in the band off the Somalian coast extending to the Arabian Sea. Other areas with elevated amplitudes can be found in shallow semi-enclosed seas and coastal regions (e.g., Indonesian seas, Hudson Bay, up to 30 cm in the Gulf of Carpentaria). Moderate annual amplitudes (3–6 cm) can be found in midlatitudes and in the North Atlantic and Mediterranean. Most of the Southern Ocean south of 45° has a weak annual signal (<3 cm).

[23] Annual phases in ζ exhibit a general reversal of seasons between northern and southern hemispheres (Figure 3b), first noted by *Patullo et al.* [1955]. Within each hemisphere, annual phases appear to be relatively homogeneous: there is no visible footprint of strong western boundary currents, and the distribution of phase contours is quite zonal. Noticeable exceptions occur in the tropics and in a few areas in the Southern Ocean. The region of elevated amplitudes in the tropical Indian Ocean, northwest of Australia, shows phase decreasing to the west, indicative of westward phase propagation of the annual cycle. Apart from the tropical Pacific (western basin; south of the equator) and possibly the tropical Atlantic (~10–20°N), there are no other regions with clear large-scale zonal propagation.

[24] At the annual frequency, ζ_ρ can be a dominant contribution to ζ. Figures 3c, 3d, 3e, and 3f show the annual amplitude and phase for the thermosteric (ζ_ρ^T) and halosteric (ζ_ρ^S) components, respectively. Annual variations in ζ_ρ^T are larger than those in ζ_ρ^S over most of the ocean and thus contribute predominantly to ζ_ρ; sizable contributions by ζ_ρ^S tend to occur in areas with large freshwater flux forcing, such as the Arabian Sea, Bay of Bengal, or along the northeast coast of South America. The annual cycle in ζ_ρ^T is quite comparable to that of ζ, for both amplitude and phase, but there are also noticeable differences besides those expected from the effects of ζ_ρ^S. For example, phases in ζ_ρ^T exhibit the same hemispheric reversal seen in ζ but have less overall skewness and regional anomalies, especially in the Southern Ocean. The strong ζ annual cycle in shallow and semi-enclosed regions is also absent in ζ_ρ^T or ζ_ρ^S. In these shallow regions, the importance of the annual cycle in ζ_m (Figures 3g and 3h) is clear.

[25] In the open ocean, the annual cycle in ζ_m is generally small (amplitude <2 cm), as also found by *Ponte* [1999], but can be similar to that in ζ in much of the Southern Ocean. The regions southwest of Australia and west of the Drake Passage (Bellingshausen Abyssal Plain) are known to have a strong barotropic variability [e.g., *Fukumori et al.*, 1998; *Stammer et al.*, 2000] at subseasonal timescales. Figure 3 indicates that, at the annual timescale, ζ variability in those regions is apparently still very much related to barotropic motions and oceanic mass redistribution. The annual phase for ζ_m, shown in Figure 3h, differs significantly from those of ζ and ζ_ρ. In particular, there is no phase reversal across the tropics, and ζ_m is nearly in-phase over most of the Pacific and Indian oceans apart from the band at 20°–40°N, similar to *Ponte* [1999].

[26] As a more quantitative analysis of the contribution of various terms to the annual cycle in ζ, we show in Figure 4 the percentage of the annual ζ variance explained by ζ_ρ^T, ζ_ρ, and ζ_m, which is computed as $(\sigma_\zeta^2-\sigma_r^2)/\sigma_\zeta^2 \times 100\%$, where σ^2 denotes variance and subscript r refers to residual series $\zeta-\zeta_\rho^T$, $\zeta-\zeta_\rho$, or $\zeta-\zeta_m$ respectively. In most of the ocean, ζ_ρ^T variability can explain more than 80% of the annual ζ variance (Figure 4a). Adding the effects of ζ_ρ^S (Figure 4b) is important in many tropical regions, particularly in the Indian Ocean, and in the northern North Pacific and North Atlantic. Exceptions to the dominance of steric effects occur at high latitudes, particularly in the Southern Ocean, where ζ_m is larger (Figure 4c) and also over many shallow coastal regions, as already noted in Figure 3. In fact, over most of the Southern Ocean, amplitude and phase differences between ζ and ζ_ρ yield negative variance explained.

[27] Insight into the contribution of different layers to ζ_ρ can be obtained by calculating the depth to which one needs to integrate steric signals from the surface to capture at least 80% of the ζ_ρ variance. Results shown in Figure 5 indicate that, over most of the extratropical oceans, the annual variability in ζ_ρ comes from the upper 100 m, suggestive of the importance of surface buoyancy fluxes. In the tropical zones, the sub-surface variability penetrates deeper (200–300 m) and in some regions can extend to much greater depths (~1000 m), pointing to the influence of advective processes and subduction related to wind driving in the

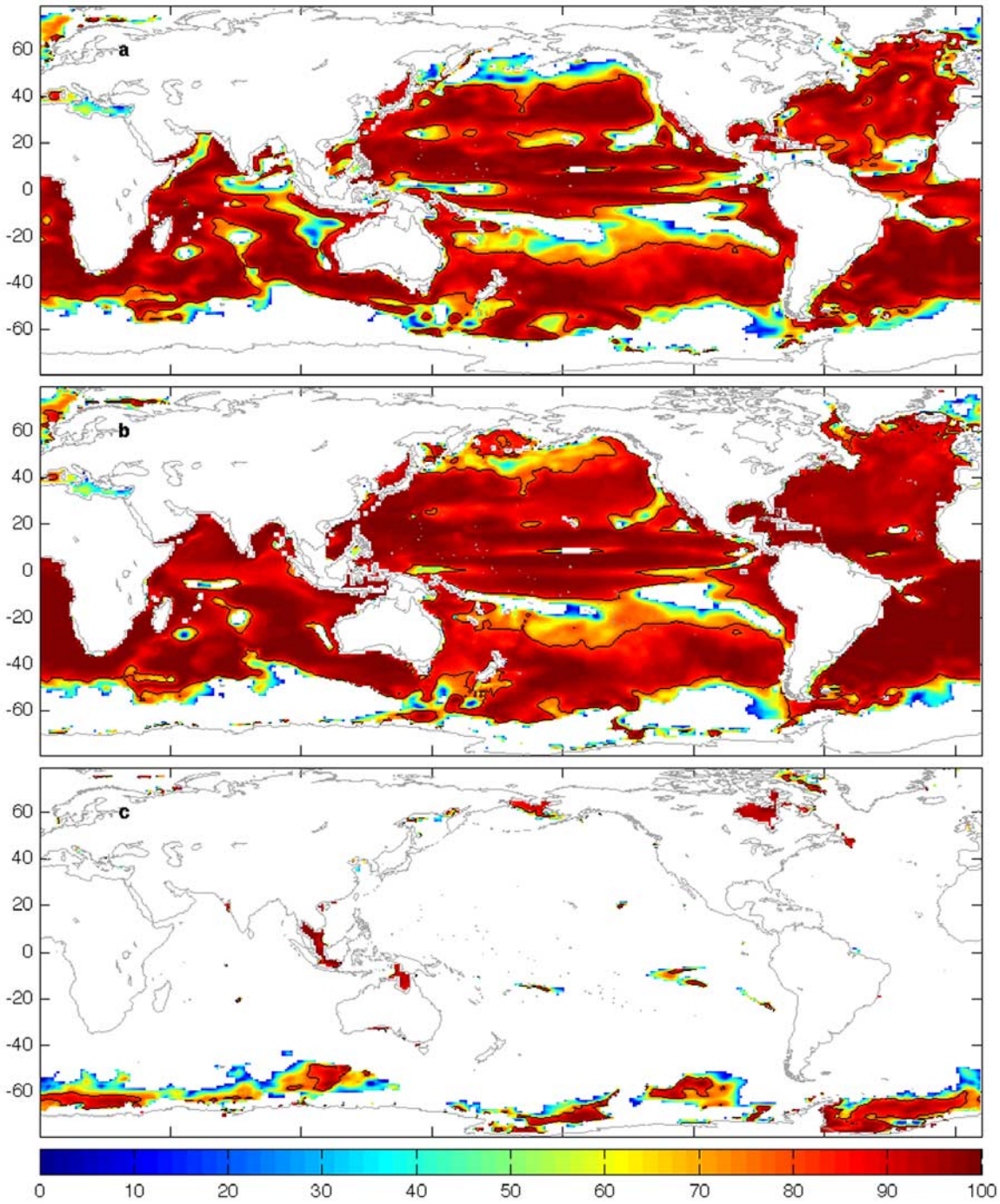

Figure 4. Percentage of variance in sea level annual cycle explained by (a) thermosteric height, (b) steric height, and (c) bottom pressure annual cycles, computed as described in the text. Solid black contour lines are plotted for a value of 80%. Blank areas denote negative values. Note that, for two signals with similar amplitude, negative values result if they are more than ~60° out of phase.

variability of ζ_ρ. Most of the regions with deep steric contributions, including those in extratropical latitudes, are places with a weak seasonal cycle relative to the background low-frequency continuum, as discussed in Figure 2, and such behavior is believed to reflect that continuum rather than the locally forced annual cycle. Particularly, in the South Pacific (~55°–70°S) and in the tropical Pacific (~0°–20°S) the annual signal does not exceed the continuum spectra.

[28] As our results are based on the climatological mean, it is important to know how much the annual cycle varies from year to year. Such variability is assessed in Figure 6 from the standard deviation of the annual cycle harmonic fits performed for each year separately. Trigonometric operations were used to assess phase variability, i.e., for a set of N phases defined as angles on the unit circle $\{u_i = \cos(\Phi_i),\ v_i = \sin(\Phi_i)\}$, $\Phi_i = \Phi(u_i, v_i)_{i=1..N}$, mean phase is $\bar{\Phi} = \arctan[\sum_{i=1}^{N} v_i / \sum_{i=1}^{N} u_i] = (\bar{u}, \bar{v})$, and standard deviation is

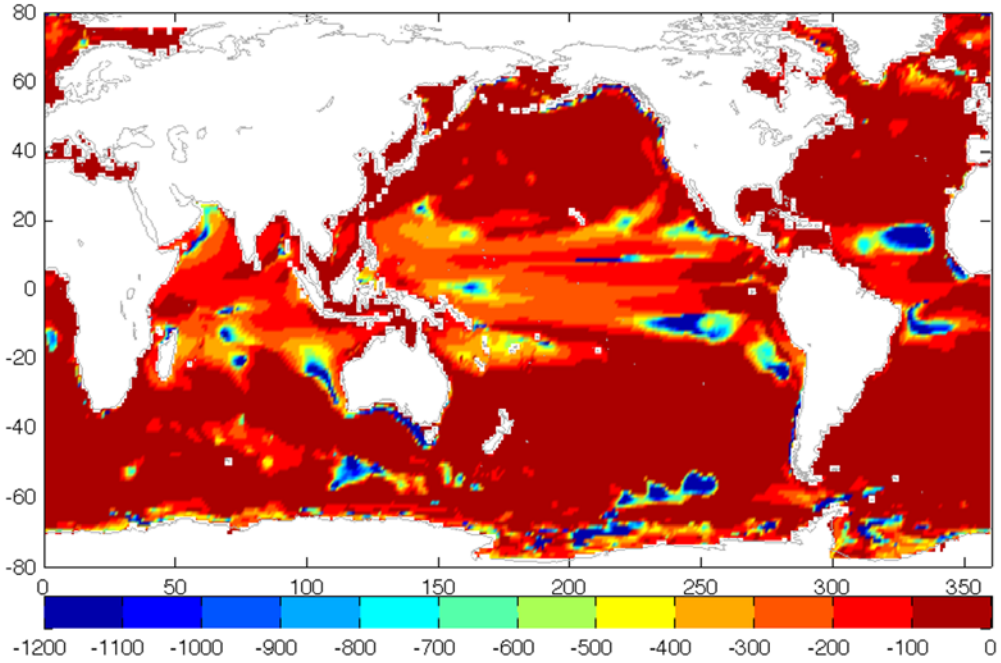

Figure 5. Depth to which it suffices to integrate the steric height signals in order to explain 80% of the total (top to bottom) annual steric height variability.

$\sigma(\Phi) = \arctan\left[\sqrt{\sum_{i=1}^{N}(v_i - \bar{v})^2}/\sqrt{\sum_{i=1}^{N}(u_i - \bar{u})^2}\right]$. Ratios of the amplitude variability to that of the mean annual cycle amplitude are generally largest (>0.2) in the tropics and also in the Southern Ocean (south of 40°S), and probably associated with the changes in the winds from year to year, as the annual cycle there is mostly wind-driven (see section 5). Relatively small amplitude changes are found in the extratropical North Pacific and North Atlantic, and at latitudes ~20°S–40°S, where surface heat fluxes tend to be most important for the annual ζ cycle (see section 5). Phase variability patterns are similar to those of amplitude, with values mostly below 45°, except in the tropics and the Southern Ocean.

[29] Figures 7a and 7b show the amplitude and phase of the semi-annual cycle in ζ. Comparison with Figures 3a and 3b reveals that the semi-annual amplitudes are in general much smaller than the annual amplitudes, except in a few areas around Antarctica, where signals are very small anyway, and in the tropics. As the seasonal ζ variability is mostly related to the annual cycle, only a brief description of the most salient features of the semi-annual cycle is given here. The largest semi-annual amplitudes are found in the Gulf of Aden (~6 cm), and high values are also observed in

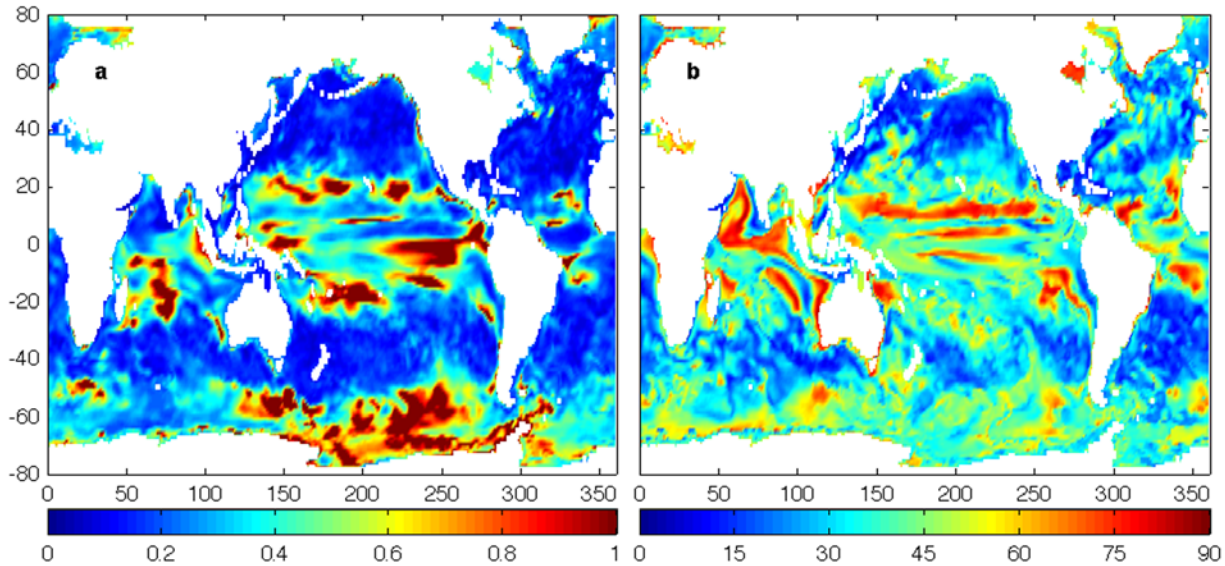

Figure 6. (a) Ratio of standard deviation of the amplitude to the mean annual amplitude and (b) the standard deviation of the annual phase in degrees, based on the sea level annual harmonics computed for each of the 13 years of record.

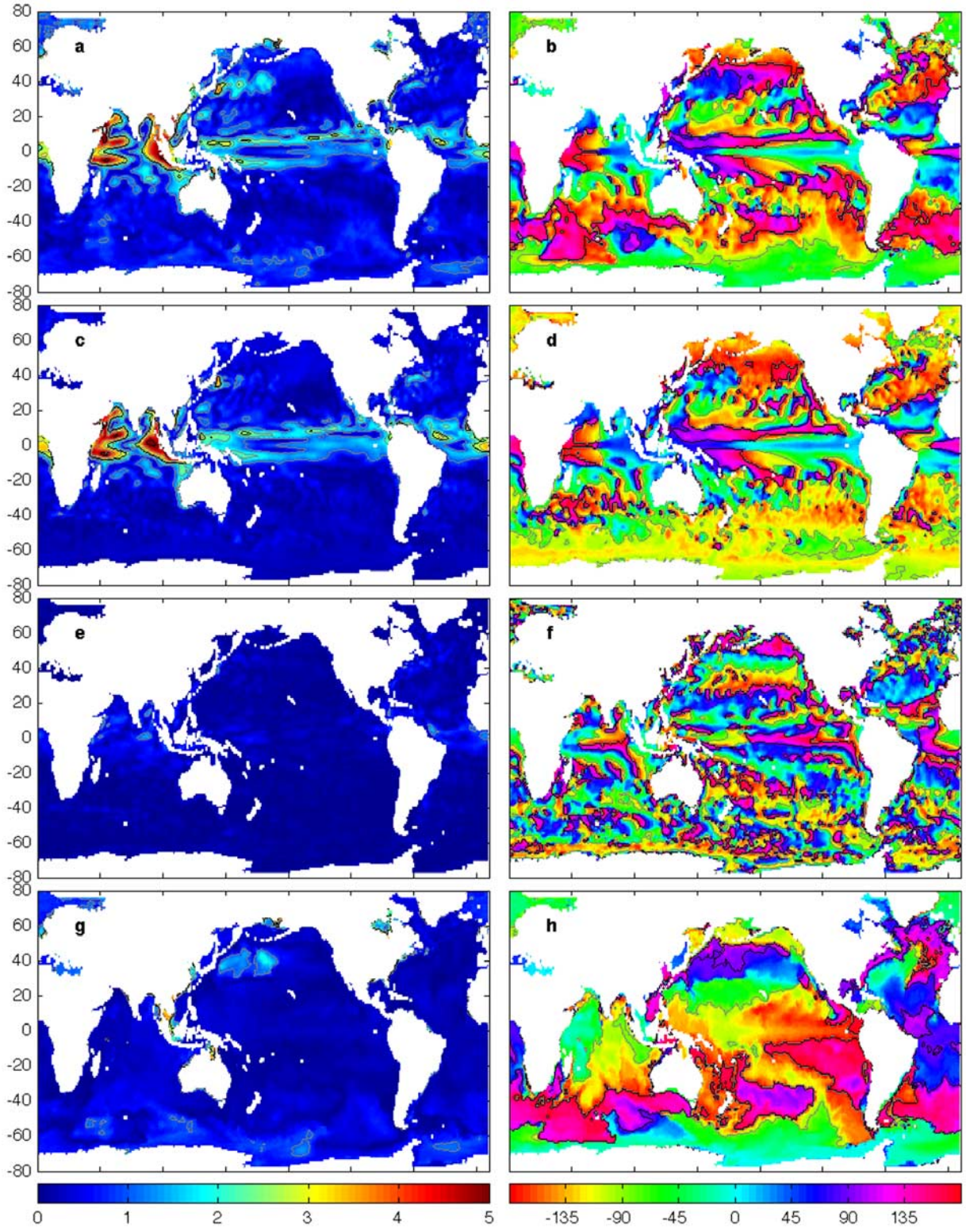

Figure 7. Same as in Figure 3 but for the semi-annual cycle in sea level. Gray contour lines are plotted every 1 cm, solid black contour lines are plotted every 2.5 cm.

other tropical areas of the Indian Ocean: east of Ninetyeast Ridge, and along the African coast north of Madagascar to the Gulf of Aden (the C-shaped amplitude feature in Figure 7a). These patterns are very consistent with the data analysis of *Fu* [2007]. Most contributions to the semi-annual cycle in ζ come from ζ_ρ^T, particularly in the regions of largest amplitudes, with ζ_ρ^S being less important and ζ_m becoming more relevant at high latitudes (Figures 7c–7h),

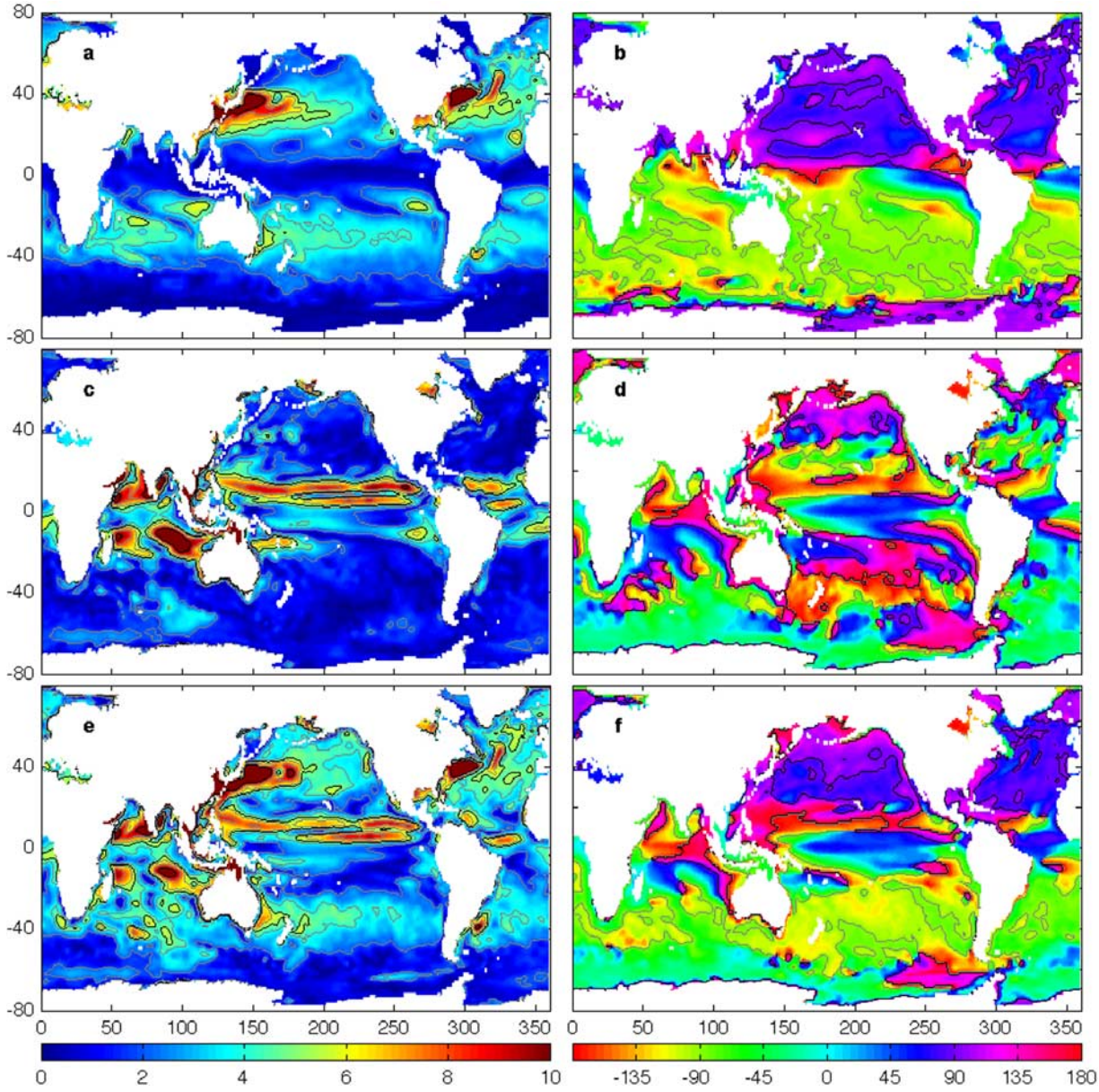

Figure 8. Amplitudes (left column, in cm) and phases (right column, in deg) of the annual cycles in sea level for the two "forcing" experiments: (a, b) all forcing fields but the heat flux set to their time mean values, and (c, d) forced in a similar way but with time-varying wind stress. In the amplitude plots, solid black contour lines are plotted every 5 cm, and gray contour lines are plotted every 2 cm. In phase plots, solid black contour lines are plotted for every 90° and gray contour lines are plotted every 45°. Bottom row shows annual amplitude (e) and phase (f) of the sum of the signals shown in Figures 8a–8d.

quite similar to the patterns for the annual cycle. Notable exception is a more pronounced contribution of ζ_m to the elevated amplitudes in northwest Pacific midlatitudes, whereas on the annual frequency, ζ_ρ variability dominates.

5. Interpretation and Discussion

[30] Numerous papers including references given in the introduction have addressed many aspects of ζ seasonal dynamics. The present discussion summarizes the general agreement of our results with previous works, while also pointing to some dynamical features of the ζ seasonal cycle that have not been much explored before. For the most part, focus is on the annual term.

5.1. Forcing Mechanisms

[31] Regional ζ variations can be forced either locally or remotely by river runoff, precipitation and evaporation, surface heat fluxes, and winds. To quantify the contribution of different forcing mechanisms to the annual cycle in ζ, we performed two numerical experiments in addition to our main run. In each of these experiments, done over the same

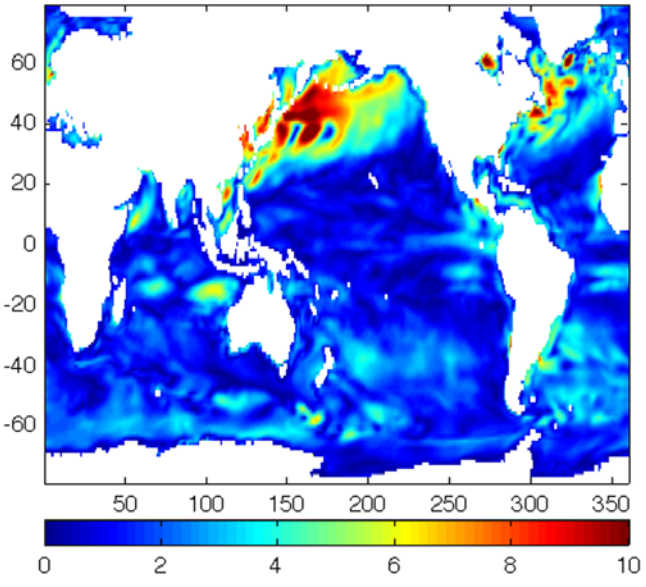

Figure 9. Amplitude (mm) of the difference in the mean annual cycle in sea level obtained from solution forced by the full-spectrum and the low-pass filtered air-sea fluxes, as described in the text.

number of years as the main run, we set all but one of the forcing fields to their time mean values at every grid point to isolate the effects of each particular forcing on the seasonal cycle. The effects of surface heat flux $\mathcal{H}$ and wind stress τ were analyzed in this manner. The annual cycles of the resulting ζ patterns are shown in Figure 8.

[32] In the experiment with $\mathcal{H}$ being the only time-varying forcing, ζ annual amplitudes (Figure 8a) are high (6–10 cm) in the vicinity of western boundary currents such as the Kuroshio and the Gulf Stream, with the latter having the strongest amplitudes (up to 14 cm). Amplitudes in Figure 8a do not exceed 5 cm in midlatitudes and are low in equatorial and high latitudes (<2 cm). The resulting annual phase (Figure 8b) shows the reversal between northern and southern hemispheres and a nearly homogeneous structure within each hemisphere. Its spatial pattern resembles the annual phase in ζ_ρ^T for the full forcing experiment (cf. Figure 3d) except south of ~65°S. In these sub-Antarctic regions, however, annual amplitudes are very small and the solution may be affected by larger uncertainties in forcing fields and the lack of a sea ice model.

[33] The τ-driven annual cycle has high amplitudes in the tropics (Figure 8c), particularly in two zonal bands between approximately 5° and 15°N in the tropical Pacific (up to 10 cm), and in the tropical Indian Ocean, particularly in areas between 10°S and 20°S (up to 13 cm) and in the Arabian Sea (up to 11 cm). Shallow and semi-enclosed seas, coastal areas and the Indian sector of the Southern Ocean southwest of Australia also have elevated annual amplitudes. In areas where amplitudes are high, the annual phases (Figure 8d) are similar to those in ζ for the full forcing experiment (cf. Figure 3b).

[34] On the large scale, the amplitude and phase of the annual cycle obtained by summing the respective cycles in the τ and $\mathcal{H}$ experiments (Figures 8e and 8f) are close to those in Figures 3a and 3b. Differences in detail (e.g., slightly different shapes and intensity of high amplitudes in the vicinity of western boundary currents) are likely related to the missing effects of freshwater flux forcing, and transient processes in the model due to slight imbalances with initial conditions when setting all but one of the forcing fields to a constant. Possible nonlinearities in the oceanic response to different kinds of forcing may also play a role, in which case ζ fields in Figure 3 are not expected to be a mere linear superposition of signals driven by τ and $\mathcal{H}$ in Figure 8. From the comparison of Figures 3 and 8, such nonlinearities appear to be small.

[35] One can thus conclude, based on Figures 3 and 8, that most ζ annual variability in midlatitudes and particularly in the vicinity of the Kuroshio and Gulf Stream is contributed by $\mathcal{H}$, whereas in the tropics and to some extent at high latitudes the annual signal is mostly τ-driven. Similar analysis of the semi-annual cycle (not shown) also point to the importance of τ for the largest signals in the tropics (Figure 7).

5.2. Nonlinear Rectification

[36] The possibility of interaction between rapid and slow timescales is an important issue in climate research. In this context, we investigated the potential effects of strong high-frequency variability in the surface atmospheric fields on the seasonal cycle in ζ, which can occur through timescale interactions allowed by the nonlinear oceanic dynamics. For this purpose, all forcing fields were low-pass filtered to remove fluctuations with periods <60 days, and the estimated ζ annual cycle was compared with that for the full forcing case. Results are displayed in Figure 9.

[37] The removal of rapid forcing leads to 10–20% changes in ζ annual amplitudes (up to ~1–2 cm) in extensive areas of the western North Pacific and North Atlantic, including the vicinity of the Kuroshio and Gulf Stream. Annual amplitudes in ζ increase on the eastern edges and decrease on the western edges of the strong geostrophic currents due to eastward shift of the main axis of these currents. Nonlinear rectification effects are expected in these regions, which have strong synoptic atmospheric variability, large annual ζ variability, and complex boundary current dynamics. (Other nonlinear effects in boundary current regions, such as those related to eddies and eddy-mean flow interactions, are not represented in our estimates, and their impact on these results remains to be studied.) Effects of similar size (in % terms) can be seen in the Southern Ocean and also in some tropical areas, although in most of these regions the annual cycle tends to be weak.

[38] Results from experiments performed by suppressing high frequencies in each forcing term one at time (not shown) indicate that rapid wind-forcing is most significant in producing rectification of the seasonal cycle (~20–40% changes in Kuroshio and Gulf Stream areas). Impact of high-frequency variability in $\mathcal{H}$ is weaker than that of τ and is most important in the western North Atlantic. These results point to the importance of including sub-monthly forcing when estimating the seasonal cycle in ζ and highlight the potential importance of nonlinearities in the ocean response to forcing. Note that rectification is not confined to the seasonal period. Similar changes to the background

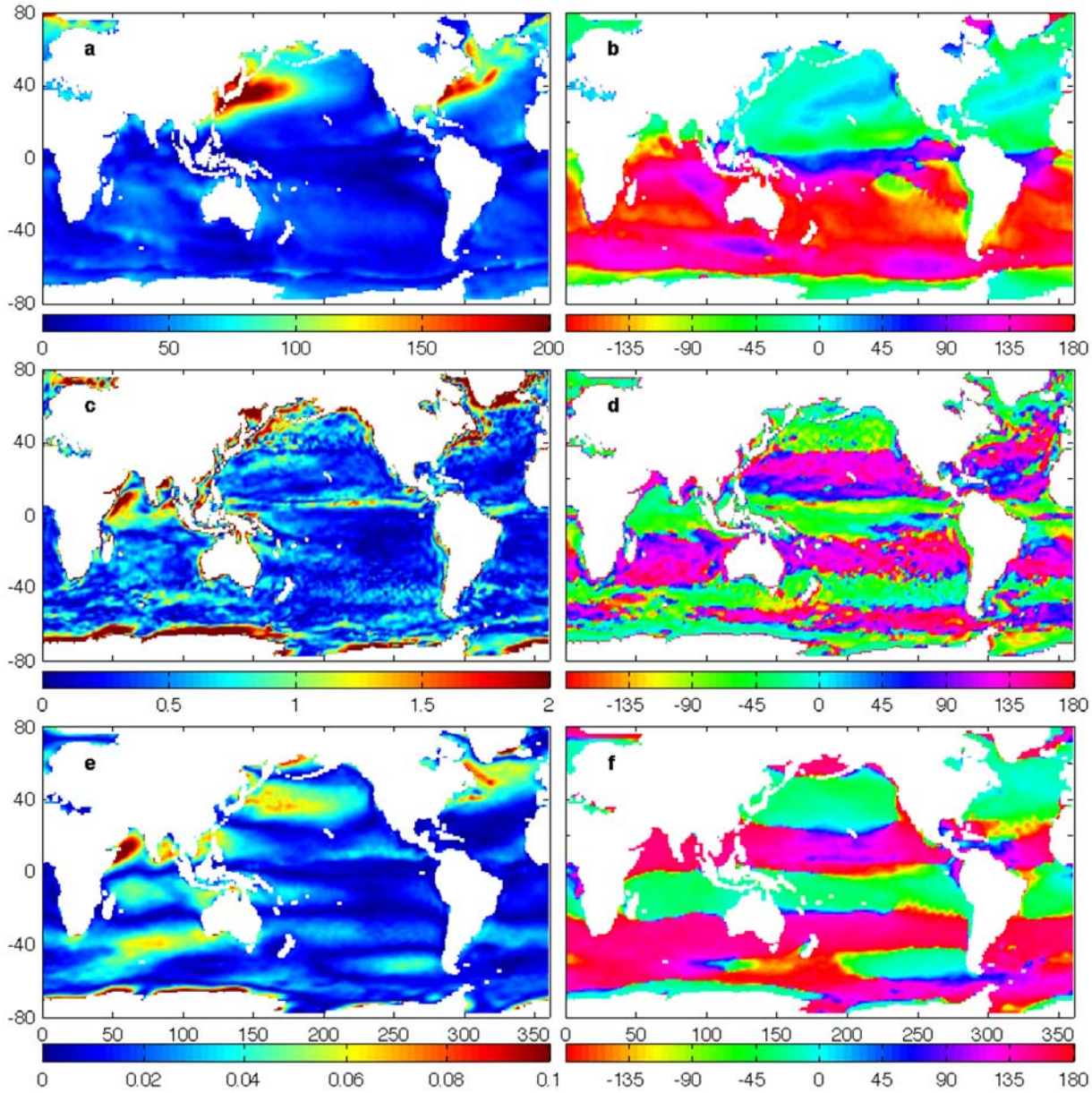

Figure 10. Amplitude and phase of the annual cycle in (a, b) surface heat flux, (c, d) wind stress curl, and (e, f) zonal wind stress. Amplitudes are in (a) Wm^{-2}, (c) 10^7 Nm^{-3}, and (e) Nm^{-2}. All phases are in degrees.

continuum are found in our results and a full investigation of these effects is left for future study.

5.3. Dynamics

[39] The complex pattern of seasonal ζ variability in Figures 3 and 7 arises from a variety of dynamic regimes in response to the relevant forcing mechanisms, particularly $\mathcal{H}$ and τ (Figure 8). The annual cycles in $\mathcal{H}$, curl of τ, which relates to vertical Ekman pumping by the wind, and zonal τ, which relates to meridional Ekman flow, are shown in Figure 10. Most of the regional maxima in the ζ annual cycle can be traced to the structure of these forcing fields.

[40] The strongest annual signals associated with western boundary current regions in the North Atlantic and Pacific are clearly related to similar patterns in $\mathcal{H}$ (Figures 10a and 10b). More generally, the annual cycle in $\mathcal{H}$ leads that of ζ (or ζ_ρ^T) by approximately 90° at mid and high latitude regions where $\mathcal{H}$ is an important driving mechanism (cf. Figure 8). Results point to a strong local heat storage effect on the annual cycle in ζ, with advection processes playing a minor role, consistent with the theory of *Gill and Niiler* [1973] and the analyses of *Stammer* [1997], *Fukumori et al.* [1998] and others. Previous studies have noted the homogenous phase of the annual cycle in $\mathcal{H}$ and the consequent large scale ζ signals with respective weak surface pressure gradients. However, Figure 10a shows large amplitude differences in the annual cycle in $\mathcal{H}$ in the western North Pacific and Atlantic. In these regions, one expects $\mathcal{H}$ to contribute to the seasonal cycle in the surface flows, as seen in the ζ response in Figures 8a and 8b.

[41] In the tropics, a more complex mixture of processes can contribute to the seasonal ζ patterns as pointed out by *Gill and Niiler* [1973]. Some of the enhanced annual ζ signals correspond well to maxima in the amplitude of the curl of τ (Figures 10c and 10d), particularly in the Arabian Sea and the Bay of Bengal, and north of the equator in the Pacific and Atlantic oceans. In these regions, vertical advection associated with local Ekman pumping can be a primary mechanism for changes in ζ_ρ^T and ζ [e.g., *Vivier et al.*, 1999; *Ferry et al.*, 2000]. In other regions, such as along the 5°S–15°S band in the Indian Ocean, other processes can be relevant, including horizontal advection by stronger Ekman flows (see zonal wind stress patterns in Figures 10e and 10f) in presence of enhanced near-surface density gradients, or remote forcing (e.g., at the eastern boundary) and Rossby wave dynamics, suggested by the presence of westward phase propagation [*Perigaud and Delecluse*, 1992; *Wang et al.*, 2001].

[42] Wave dynamics is generally most important in the tropics [e.g., *Vivier et al.*, 1999]. Annual phases in Figure 3b exhibit various propagation patterns, including bending of phase lines with latitude characteristic of so-called β-refraction of Rossby waves. Wave propagation can also be very important at the semi-annual period. The patterns of semi-annual variability in the tropical Indian Ocean (Figure 7) result from the complex interaction of equatorial Kelvin and Rossby waves, with boundary reflections leading to a large-scale basin mode resonance with a nodal point in the center of the tropical Indian Ocean [*Fu*, 2007]. In contrast, the lack of phase propagation in ζ, noted in Figure 3b at mid and high latitudes, reflects in part the dominance of large-scale heat storage effects already discussed, and also the expected quasi-static Sverdrup balance response to wind-forcing as argued by *Willebrand et al.* [1980]. Annual phase propagation becomes more apparent at mid latitudes when examining results with wind driving only (Figure 8d), particularly near eastern boundary regions, which tend to be significant sources of baroclinic annual Rossby waves [*Krauss and Wuebber*, 1982]. Note, however, that some of the annual baroclinic Rossby wave signals at mid latitudes may not be well resolved by our 1° grid [e.g., *Cummins et al.*, 1986]. At the large scales considered by *Gill and Niiler* [1973], little wave propagation is expected, consistent with our results.

[43] Figure 8 also shows the tendency for heat flux-driven effects in the tropics to generally reduce the amplitude of the wind-driven signals. Such behavior is best seen, for example, in the reduced maxima in the tropical Pacific and eastern tropical Indian Ocean (cf. Figures 8c and 8e). The results are consistent with a dynamic ocean response to winds that produces correlated annual anomalies in ζ and ζ_ρ^T, and thus in upper ocean heat content or sea surface temperature, and a response of the tropical atmosphere to these upper ocean heat anomalies that tends to dampen them and reduce ζ. This is in contrast with the annual cycle in the extratropics, with the ocean responding more passively to large seasonal changes in air temperatures and the resulting strong annual $\mathcal{H}$ fluctuations.

[44] Bathymetric effects shape the seasonal ζ cycle in at least two important ways. *Gill and Niiler* [1973] pointed out the possible importance of closed f/H contours in altering seasonal dynamics. Evidence for the importance of such effects, as revealed by enhanced contributions by ζ_m term to ζ, are seen in the northwest Pacific (~45°N) and in the Southern Ocean, southwest of Australia, in areas known to have weakened f/H gradients, and where wind driving becomes more important [*Vivier et al.*, 1999, 2005]. In addition, our results indicate that, over wide shelf regions, seasonal variability in coastal and deep ocean ζ can be very different. As wind stress acts over a much thinner layer, barotropic wind-driven ζ_m effects over shallow depths tend to dominate over ζ_ρ variability, contrary to what happens in deeper contiguous areas. This behavior can explain the differences found between the seasonal cycle in coastal ζ and nearby ζ_ρ by *Patullo et al.* [1955] and is apparently common to other timescales as well [*Vinogradova et al.*, 2007].

6. Summary

[45] We have explored the general characteristics of the seasonal cycle in ζ using an ocean climatology for the period 1992–2004 based on the ECCO-GODAE optimization procedure, which fits the MIT general circulation model to most available ocean data in a least squares sense. Variability in $\overline{\zeta}$ is only a few mm in amplitude and primarily related to somewhat canceling effects of $\overline{\zeta_\rho^T}$ and $\overline{\zeta_m}$ at the annual timescale. Regionally, the ζ seasonal cycle exhibits rich amplitude and phase patterns, with several maxima in the tropics and in the western parts of most basins, as well as in shallow coastal regions, and phase structures of increasing complexity as one moves equatorward. Most of the seasonal cycle in tropical and midlatitudes is explained by near-surface thermosteric effects, but contributions from deeper layers as well as from halosteric effects are not negligible in some locations. In the Southern Ocean and some shallow coastal areas, seasonal bottom pressure signal is large, implying that ocean mass redistribution processes have a major role in the ζ seasonal variability. Forcing by τ is important in the tropics and high latitudes, and $\mathcal{H}$ contributes mostly at midlatitudes, with the effects of τ and $\mathcal{H}$ acting approximately in linear superposition. The ζ seasonal cycle in areas with large signals and strong atmospheric synoptic systems, such as the western North Atlantic and North Pacific, were found to depend substantially on the presence of the submonthly variability in the forcing fields, which implies some degree of nonlinear rectification.

[46] The ECCO-GODAE ζ climatology explored here is arguably a "best" representation of the mean oceanic state for the period from the beginning of the altimetric observations. Such estimates are very useful because they are nearly global, physically consistent with the model dynamics and forcing fields, and close to most available data within expected uncertainties. As such, they can be analyzed quantitatively in much more detail than was possible in this global characterization of the ζ seasonal cycle, for any region of interest. One caveat of the present work is the lack of a complete estimate of uncertainty, for which one needs much better understanding of all model errors; ensemble and other methods are in the early trial stages and may yield results in the future. Lack of resolution is a particularly relevant model deficiency because it affects the ability to estimate coastal signals, as seen for example by tide gauges. Ongoing plans for higher resolution will permit

the efficient use of information in tide gauge records as a further constraint on the solutions. The ECCO-GODAE estimates will continue to improve with new data, model physics, resolution, etc., and their examination should lead to better understanding of the large-scale mechanisms that control seasonal and lower frequency ζ variability. This work is intended to spur further exploration of the ECCO-GODAE estimates by the oceanographic community; a number of publicly available ECCO-GODAE solutions can be found at www.ecco-group.org.

[47] **Acknowledgments.** We thank our ECCO-GODAE and MITgcm colleagues for help with all data sets and modeling runs. ECCO-GODAE is supported by the National Ocean Partnership Program (NOPP) of NASA, NSF, and NOAA. Support by NASA Jason-1 Project through AER contract 1206432 with the Jet Propulsion Laboratory is also acknowledged. We are grateful for the continued access to computing resources at GFDL (for ECCO-GODAE production), NCAR and NASA/ARC (for diagnostic and sensitivity experiments).

References

Chambers, D. P., J. Wahr, and R. S. Nerem (2004), Preliminary observations of global ocean mass variations with GRACE, *Geophys. Res. Lett.*, *31*, L13310, doi:10.1029/2000GL006119.

Chen, J. L., C. R. Wilson, D. P. Chambers, R. S. Nerem, and B. D. Tapley (1998), Seasonal global water mass budget and mean sea level variations, *Geophys. Res. Lett.*, *25*, 3555–3558.

Chen, J. L., C. R. Wilson, B. D. Tapley, J. S. Famiglietti, and M. Rodell (2005), Seasonal global mean sea level change from satellite altimeter, GRACE, and geophysical models, *J. Geod.*, *79*, 532–539.

Cummins, P. F., L. A. Mysak, and K. Hamilton (1986), Generation of annual Rossby waves in the North Pacific by the wind stress curl, *J. Phys. Oceanogr.*, *16*(7), 1179–1189.

Fernandes, M. J., S. Barbosa, and C. Lázaro (2006), Impact of altimeter data processing on sea level studies, *Sensors*, *6*, 131–163.

Ferry, N., G. Reverdin, and A. Oschlies (2000), Seasonal sea surface height variability in the North Atlantic, *J. Geophys. Res.*, *105*, 6307–6326.

Fu, L.-L. (2007), Intraseasonal variability of the equatorial Indian Ocean observed from sea surface height, wind, and temperature data, *J. Phys. Oceanogr.*, *37*(2), 188–202.

Fu, L.-L., and R. D. Smith (1996), Global ocean circulation from satellite altimetry and high-resolution computer simulation, *Bull. Am. Meteorol. Soc.*, *77*, 2625–2636.

Fukumori, I., R. Raghunath, and L.-L. Fu (1998), Nature of global large-scale sea level variability in relation to atmospheric forcing: A modeling study, *J. Geophys. Res.*, *103*, 5493–5512.

Gill, A. E., and P. P. Niiler (1973), The theory of the seasonal variability in the ocean, *Deep Sea Res.*, *20*, 141–177.

Halliday, D., R. Resnick, and J. Walker (2004), *Fundamentals of Physics*, 7th ed., 1136 pp., Wiley.

Heimbach, P., C. Hill, and R. Giering (2005), An efficient exact adjoint of the parallel MIT general circulation model, generated via automatic differentiation, *Future Generation Computer Systems (FGCS)*, *21*(8), 1356–1371, doi:10.1016/j.future.2004.11.010.

Heimbach, P., R. M. Ponte, C. Evangelinos, G. Forget, M. Mazloff, D. Menemenlis, S. Vinogradov, and C. Wunsch (2006), Combining altimetric and all other data with a general circulation model, *15 Years of Progress in Radar Altimetry Symposium*, Venice, 13–18 March 2006, ESA Spec. Pub. SP-614.

Jacobs, G. A., G. H. Born, M. E. Parke, and P. C. Allen (1992), The global structure of the annual and semiannual sea surface height variability from Geosat altimeter data, *J. Geophys. Res.*, *97*(C11), 17,813–17,828, doi:10.1029/92JC01708.

Kalnay, E., et al. (1996), The NCEP/NCAR 40-year reanalysis project, *Bull. Am. Metereol. Soc.*, *77*, 437–471.

Krauss, W., and C. Wuebber (1982), Response of the North Atlantic to annual wind variations along the eastern coast, *Deep Sea Res.*, *29*, 851–864.

Levitus, S., and T. P. Boyer (1994), World Ocean Atlas 1994, NOAA Atlas NESDIS, NOAA, Silver Spring, MD.

Lombard, A., D. Garcia, G. Ramillien, A. Cazenave, R. Biancale, J. M. Lemoine, F. Flechtner, R. Schmidt, and M. Ishii (2007), Estimation of steric sea level variations from combined GRACE and Jason-1 data, *Earth Planet. Sci. Lett.*, *254*, 194–202, doi:10.1016/j.epsl.2006.11.035.

Marshall, J., A. Adcroft, C. Hill, L. Perelman, and C. Heisey (1997a), A finite-volume, incompressible Navier Stokes model for studies of the ocean on parallel computers, *J. Geophys. Res.*, *102*, 5753–5766.

Marshall, J., C. Hill, L. Perelman, and A. Adcroft (1997b), Hydrostatic, quasi-hydrostatic and non-hydrostatic modeling, *J. Geophys. Res.*, *102*, 5733–5752.

Minster, J. F., A. Cazenave, Y. V. Serafini, F. Mercier, M. C. Gennero, and P. Rogel (1999), Annual cycle in mean sea level from Topex-Poseidon and ERS-1: Inference on the global hydrological cycle, *Global Planet. Change*, *20*, 57–66.

Munk, W. (2003), Ocean freshening, sea level rising, *Science*, *300*, 2041–2043.

Patullo, J. G., W. H. Munk, R. Revelle, and E. Strong (1955), The seasonal oscillation in sea level, *J. Mar. Res.*, *14*, 88–155.

Perigaud, C., and P. Delecluse (1992), Annual sea level variations in the southern tropical Indian Ocean from Geosat and shallow water simulations, *J. Geophys. Res.*, *97*, 20,169–20,178.

Pierini, S. (2003), A model of the wind-driven seasonal variability in the tropical North Pacific, with validation through altimeter data, *J. Phys. Oceanogr.*, *33*, 2156–2172.

Ponte, R. M. (1999), A preliminary model study of the large-scale seasonal cycle in bottom pressure over the global ocean, *J. Geophys. Res.*, *104*, 1289–1300.

Ponte, R. M. (2006), Low-frequency sea level variability and the inverted barometer effect, *J. Atmos. Oceanic Tech*, *23*, 619–629.

Ponte, R. M., C. Wunsch, and D. Stammer (2007a), Spatial mapping of time-variable errors in Jason-1 and TOPEX/POSEIDON sea surface height measurements, *J. Atmos. Oceanic Technol.*, *24*, 1078–1085.

Ponte, R. M., K. J. Quinn, C. Wunsch, and P. Heimbach (2007b), A comparison of model and GRACE estimates of the large-scale seasonal cycle in ocean bottom pressure, *Geophys. Res. Lett.*, *34*, L09603, doi:10.1029/2007GL029599.

Siedler, G., J. Church, and J. Gould (2001), *Ocean circulation and climate: Observing and modeling the global ocean*, AIP Int. Geophys. Series, vol. 77, 715 pp., Academic Press.

Stammer, D. (1997), Steric and wind-induced changes in TOPEX/POSEIDON large-scale sea surface topography observations, *J. Geophys Res.*, *102*(C9), 20,987–21,009.

Stammer, D., C. Wunsch, and R. M. Ponte (2000), De-aliasing of global high frequency barotropic motions in altimeter observations, *Geophys. Res. Lett.*, *27*, 1175–1178.

Stephens, C. J., I. Antonov, T. P. Boyer, M. E. Conkright, R. Locarnini, and T. D. O'Brien (2002), World Ocean Atlas 2001, NOAA Atlas NESDIS 49, NOAA, Silver Spring, MD.

Tsimplis, M. N., and P. L. Woodworth (1994), The global distribution of the seasonal sea level cycle calculated from coastal tide gauge data, *J. Geophys. Res.*, *99*(C8), 16,031–16,039.

Vinogradova, N. T., R. M. Ponte, and D. Stammer (2007), Relation between sea level and bottom pressure and the vertical dependence of oceanic variability, *Geophys. Res. Lett.*, *34*, L03608, doi:10.1029/2006GL028588.

Vivier, F., K. A. Kelly, and L. Thompson (1999), Contributions of wind forcing, waves, and surface heating to sea surface height observations in the Pacific Ocean, *J. Geophys. Res.*, *104*(C9), 20,767–20,788.

Vivier, F., K. A. Kelly, and M. Harismendy (2005), Causes of large-scale sea level variations in the Southern Ocean: Analyses of sea level and a barotropic model, *J. Geophys. Res.*, *110*, C09014, doi:10.1029/2004JC002773.

Wang, L., C. Koblinsky, and S. Howden (2001), Annual Rossby wave in the Southern Indian Ocean: Why does it "appear" to break down in the middle ocean?, *J. Phys. Oceanogr.*, *31*, 54–74.

Willebrand, J., S. G. H. Philander, and R. C. Pacanowski (1980), The oceanic response to large-scale atmospheric disturbances, *J. Phys. Oceanogr.*, *10*, 411–429.

Wunsch, C. (1967), The long-period tides, *Rev. Geophys.*, *5*, 447–475.

Wunsch, C., and P. Heimbach (2006), Estimated decadal changes in the North Atlantic meridional overturning circulation and heat flux 1993–2004, *J. Phys. Oceanogr.*, *26*, 2012–2024.

Wunsch, C., and P. Heimbach (2007), Practical global oceanic state estimation, *Physica D*, *230*, 197–208.

Wunsch, C., R. M. Ponte, and P. Heimbach (2007), Decadal trends in sea level patterns: 1993–2004, *J. Clim.*, *20*, 5889–5911, doi:10.1175/2007JCLI1840.1.

P. Heimbach and C. Wunsch, Massachusetts Institute of Technology, Cambridge, MA, USA.

R. M. Ponte and S. V. Vinogradov, Atmospheric and Environmental Research, Inc., 131 Hartwell Ave., Lexington, MA 02421, USA. (sergey@aer.com)